

Nanodiamonds based optical-fiber quantum probe for magnetic field and biological sensing

Yaofei Chen^{1,2}, Qianyu Lin^{1,2}, Hongda Cheng^{1,2}, Yingying Ye², Gui-Shi Liu^{1,2}, Lei Chen^{1,2}, Yunhan Luo^{1,2,3*}
Zhe Chen^{1,2,3}

1 Guangdong Provincial Key Laboratory of Optical Fiber Sensing and Communications, Jinan University, Guangzhou 510632, China

2 Department of Optoelectronic Engineering, Jinan University, Guangzhou 510632, China

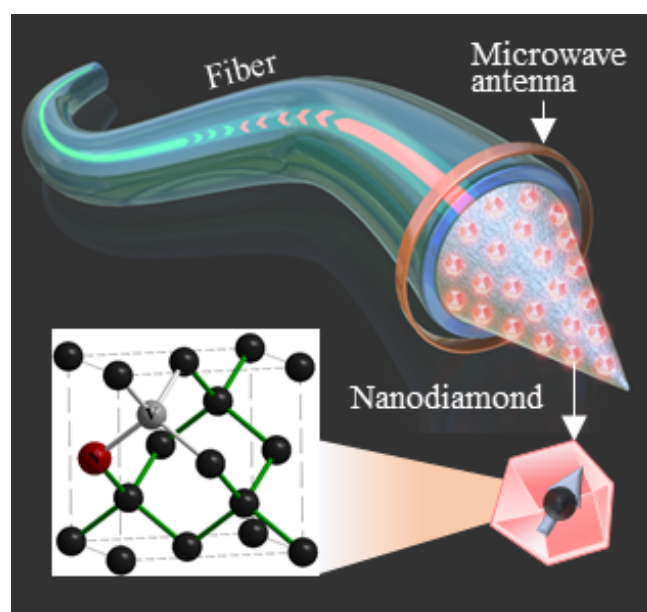
3 Key Laboratory of Optoelectronic Information and Sensing Technologies of Guangdong Higher Educational Institutes, Jinan University, Guangzhou 510632, China

* Corresponding author: Yunhan Luo, yunhanluo@163.com

Abstract

Owing to the unique electronic spin properties, the nitrogen-vacancy (NV) centers hosted in diamond have emerged as a powerful quantum sensor for various physical parameters and biological species. In this work, a miniature optical-fiber quantum probe, configured by chemically-modifying nanodiamonds NV centers on the surface of a cone fiber tip, is developed. Based on continue-wave optically detected magnetic resonance method and lock-in amplifying technique, it is found that the sensing performance of the probe can be engineered by varying the nanodiamonds dispersion concentration and modification duration in the chemical modification process. Combined with a pair of magnetic flux concentrators, the magnetic field detection sensitivity of the probe is significantly enhanced to $0.57 \text{ nT/Hz}^{1/2} @ 1\text{Hz}$, a new record among the fiber magnetometers based on nanodiamonds NV. Taking Gd^{3+} as the demo, the capability of the probe in paramagnetic species detection is also demonstrated experimentally. Our work provides a new approach to develop NV center as quantum probe featuring high integration, miniature size, multifunction, and high sensitivity, etc.

KEYWORDS: Quantum probe, cone optical-fiber tip, nanodiamonds, nitrogen-vacancy centers.



INTRODUCTION

In recent years, the quantum sensing based on diamond nitrogen-vacancy (NV) centers had gained increasing attentions and developments. The negatively-charged NV (unless specified, NV refers to the negative charge state in this paper) belongs to one of 500 different color centers discovered in diamond, and it owns the unique properties such as the ideal photostability without photobleaching, optically-readable electronic spin state at room-temperature, and excellent biocompatibility¹. Most of the parameters that are able to affect the spin state of NV can be easily detected through the optically detected magnetic resonance (ODMR) method. In the aspect of sensing to physical parameters such as magnetic field, temperature, and electric field, the NV⁻ based sensors have shown great advantages. For example, compared to the well-known superconducting quantum interference device (SQUID) magnetometer, the well-designed NV magnetometers not only possess the comparable sensitivity but can work at room temperature as well². Furthermore, the tetrahedral structure of the diamond crystal lattice enables such magnetometer to directly sense a magnetic field vector, an advantage over the inherently scalar measurements of traditional atomic magnetometers³. Employing the nanodiamonds (NDs) containing NV even allows us to measure the intracellular thermal conductivity in situ⁴, which is almost impossible for the traditional sensors. Recently, NV centers had also been proved as a breakthrough tool in the biomedical sensing, though currently it is in its infancy⁵. Utilizing the microwave (MW) or magnetic-field-tunable emission intensity of NV centers and the frequency-domain analysis method, the sensitivity of lateral flow immunoassays succeeded to be improved to an unprecedented level⁶, enabling the single-copy detection of HIV-1 RNA⁷. Particularly, the NV centers have shown great potentials for the detection of the physiologically relevant species (e.g. free radicals, paramagnetic molecules, and ions)⁸⁻¹⁰ and pH^{11,12}, which play an essential role in various critical biological processes, in a label-free manner. For example, Y. Ninio et.al realized a high sensitivity detection to hydroxyl radical by exploiting the fluorescence difference between NV charged states⁸. The detection limit down to the nanomolar range for free radicals had also been achieved while adopting the T1 relaxation measurement⁹. This further provides a promising method to exploring the localized chemical events¹³ or chemical redox processes¹⁴, in which the free radicals or paramagnetic species are incorporated. In a word, the NV centers hosted in diamond have been demonstrated as an ideal quantum probe for the detection to various physical parameters and biological species.

During the implementation of NV⁻ based sensor, the generally-adopted form is space light coupling¹⁵, i.e. using a microscope objective or lens to focus the pump laser on the diamond NV, and the emitted fluorescence is collected by the same or additional device. This form is flexible and easy to implement, but the integration of the resulted sensor is poor. Although the recent works had made a big progress on the compactness and portability^{16,17}, it is at the expense of spatial resolution, since a long-distance separation between the sensing head and the required optical elements (such as the lens, filter, dichroic mirror) is infeasible for the space light coupling form. A promising solution is to employ the optical-fiber integration form, which exploits the unique features of fiber (e.g. flexible optical path, enabling long-distance light transmission, and small size) and guarantees the high spatial resolutions and integration at the same time. The optical-fiber integration form had been successfully implemented by adhering a diamond block or particle on the fiber facet¹⁸⁻²², or filling the micron diamond particles suspension into the air holes of a hollow core fiber²³, or physically-depositing the NDs on the surface of tapered fiber^{24,25}. Nevertheless, the sensitivity of this kind of sensors is not high. Especially for the NDs-integrated fiber magnetometers^{24,25},

the sensitivity has not broken below $10 \mu\text{T}/\text{Hz}^{1/2}$ so far. Moreover, their applications to the biosensing have not been explored.

In this paper, we developed a novel optical-fiber quantum probe incorporated with NDs NV centers, and applied it to the detection of magnetic field and paramagnetic species, respectively. The probe was constructed by modifying the NDs onto the surface of a conical fiber tip through chemical covalent bonding. The influence of two key parameters, i.e. the NDs dispersion concentration (DC) and modification duration (MD) used in modification process, were well studied. Combined with a magnetic flux concentrator, the magnetic field detection sensitivity of the probe was successfully enhanced to sub-nT/Hz^{1/2} at 1 Hz, which is the highest sensitivity among the reported fiber magnetometers based on NDs. The capability of the probe in paramagnetic species sensing was also proved experimentally.

METHODS AND MATERIALS

The proposed probe [schematically shown by figure 1(a)] is composed of a multi-mode fiber (MMF) with a conical tip, whose surface is modified with NDs carrying NV centers. NV centers are such a kind of defects in diamond lattice that a carbon atom is substituted by a nitrogen atom and a vacancy appears at its adjacent site [Figure 1(b)]. The fundamental for magnetic field sensing lies on the spin-triplet ground state ³A₂ of NV and the Zeeman effect [Figure 1(c)]. In the absence of external magnetic field, the doublet ms=±1 states (denoted by |±1>) are degenerate, and an intrinsic separation of $D = 2.87\text{GHz}$ occurs between the |±1> and singlet |0> resulting from the spin-spin interaction. Once an external magnetic field is applied, the originally degenerate |±1> will split due to the Zeeman effect, and the splitting degree $\Delta\nu$ is proportional to the magnetic field projected along the NV symmetry axis (denoted by B_{NV}), which can be expressed as $\Delta\nu = 2\gamma_e B_{\text{NV}}$, where $\gamma_e = 28\text{GHz/T}$ is the NV gyromagnetic ratio.

The spin-state-dependent fluorescence intensity of NV allows us to exactly measure the $\Delta\nu$ via the ODMR method, thus obtaining the BNV. To achieve this, a green laser is used to pump the NV from ground state ³A₂ to the excited state ³E obeying spin conservation, and then decays back the ground state while emitting red fluorescence. Different from that the excited |0> totally returns back the ground |0>, a part of excited |±1> will return to the ground |0> through the non-radiative path, meaning that the |±1> emits a darker fluorescence and NV will be ultimately polarized to the ground |0> by laser pump. At the same time, if a MW is exerted on the NV and its frequency is matched with that between |0> and |+1> (or |-1>), the |0> will be partly depolarized to |+1> (or |-1>), resulting in the decrease of fluorescence. Consequently, by monitoring the fluorescence while sweeping the MW frequency, we can obtain the ODMR spectrum [as shown in Figure 1(d)], which features two dips centered at the frequency ν_+ and ν_- , corresponding to the transitions of |0> ↔ |+1> and |0> ↔ |-1>. Thus, the $\Delta\nu = |\nu_+ - \nu_-|$ as well as the B_{NV} can be achieved.

The used conical optical-fiber tip, fabricated by chemically-etching a step-index silica MMF (SI2014-N, YOFC, with the core/cladding diameter of 105/125 μm), was observed under an optical microscope (MJ30, Guangzhou Mshot Co.), and the taper length was measured as 270 μm [Figure 1(e)]. The fluorescent carboxylated-NDs (purchased from FND Biotech. Inc.) were characterized by scanning electron microscope (SEM), fourier transform infrared spectroscopy (FTIR, Shimadzu), and photoluminescence spectroscopy (Horiba scientific), respectively. The SEM image [Figure 1(f)] indicates that the NDs have the cube-like morphology and a diameter 100 nm. The FTIR spectrum [Figure 1(g)] features the dips located at 1635 and 3428 cm⁻¹ (attributed to O-H stretching vibrations) and 1735 cm⁻¹ (induced by C=O bending vibrations), confirming the modification of carboxyl group on the NDs surface²⁶. Besides, other chemical bond features,

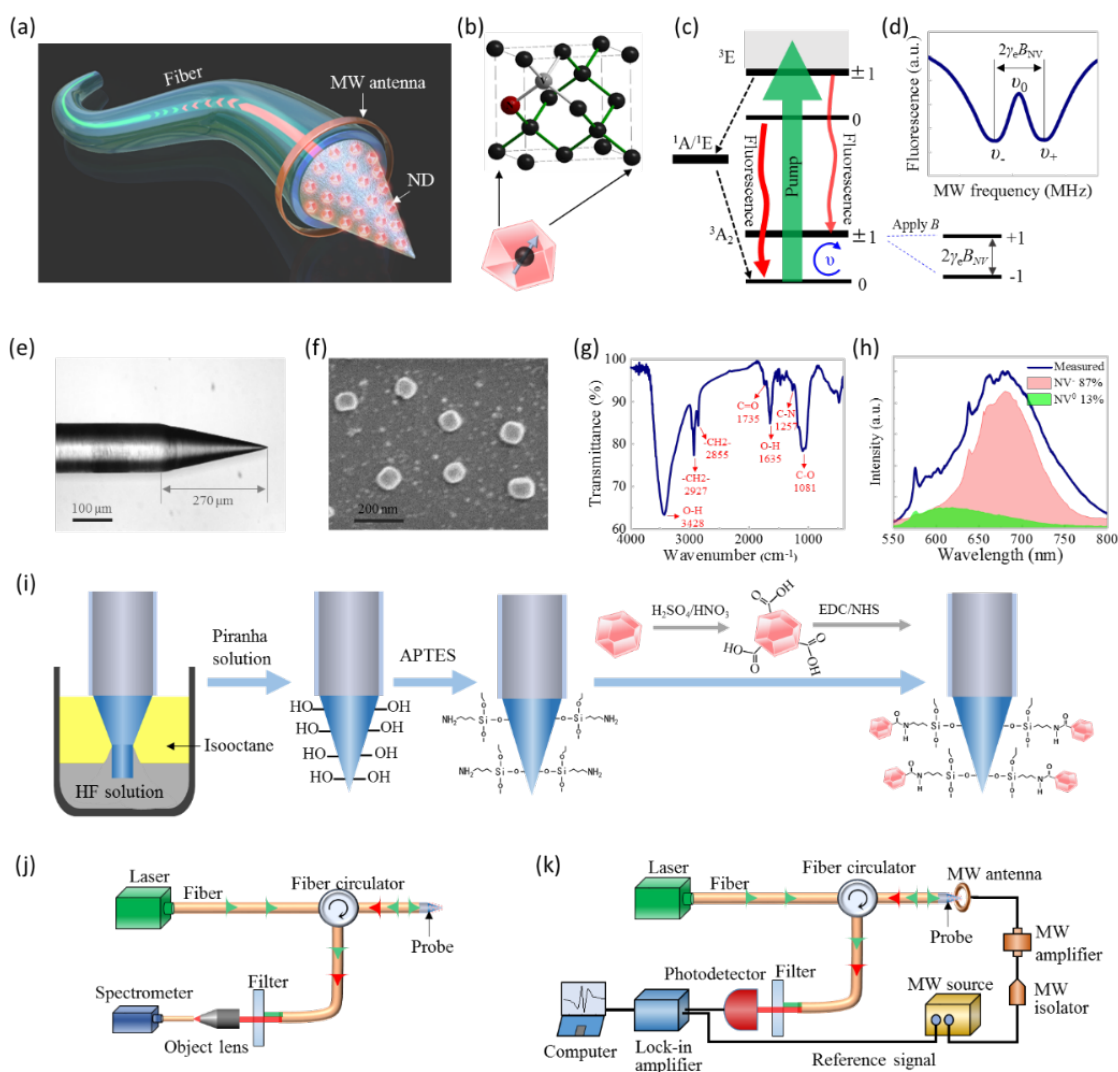


Figure 1. (a) Schematic representation of the optical-fiber quantum probe. It consists of a fiber with conical tip, the NDs modified on the tip, and a MW antenna wound around the tip. (b) The NV defect presented in the diamond lattice. (c) Energy-level structure, including the paths of laser pump and fluorescence emission, MW induced magnetic resonance between $|0\rangle$ and $|\pm 1\rangle$, and the magnetic field induced split of $|\pm 1\rangle$, for NV center. (d) Schematic diagram of ODMR spectrum. (e) Microscope image for the bare conical fiber tip. (f)-(h) SEM image, FTIR spectrum, and photoluminescence spectrum (using 532 nm light for excitation) of NDs. (i) Schematic diagram of probe preparation process. (j) Schematic diagram of the test setup for fluorescence spectrum. (k) Schematic diagram of the measurement setup for lock-in ODMR spectrum. During measurements, the same parameters, including the MW scan range (2820-2920 MHz), scan step (0.5 MHz), dwell time (500 ms), frequency modulation deviation (2 MHz), modulation frequency (500 Hz), lock-in time constant (100 ms), filter roll-off (12 dB/oct), and the gain of the photodetector, etc., were chosen for different probes.

including the C-O stretching vibrations at 1081 cm^{-1} , C-N bending vibrations at 1257 cm^{-1} (corresponding to the nitrogen-induced defects in NDs), and the symmetric and antisymmetric stretching vibrations of the CH₂ groups at 2855 cm^{-1} and 2927 cm^{-1} , can also be observed in the FTIR spectrum²⁶. The measured photoluminescence spectrum [Figure 1(h)] shows the fluorescence band of NDs ranging from 550 to 800 nm, among which two peaks located at 575 and 637 nm, corresponding to the zero photon lines of NV⁰ and NV⁻, are clearly seen. Furthermore, by deconvoluting the measured spectrum into the two pure spectra of NV⁰ and NV⁻²⁷, we can evaluate the percentage of NV⁻ as 87%.

As depicted in Figure 1(i), the probe was fabricated by the following four steps. *I.* A piece of MMF (>40 cm in length) was first cut to obtain a flat end face. Then, the fiber was immersed in the 40% HF solution covered by a thin layer of isooctane for 1.5 hours. The HF solution reduced the fiber diameter by chemically-etching while the isooctane prevented fiber from being etched, which finally resulted in the formation of a cone fiber tip. The obtained cone tip was sufficiently rinsed by ethanol and deionized water. *II.* Immersed the cone tip in piranha solution (mixture of H₂SO₄ and H₂O₂ with the volume ratio of 7:3) for 30 minutes to hydroxylate the surface. Then, cleaned the tip using deionized water and dried it under 100 °C. *III.* Incubated the hydroxylated fiber tip in the (3-aminopropyl)-triethoxysilane (APTES) ethanol solution (1:10 in volume) for 5 hours to further aminate the surface, which was followed by sufficiently rinsing using ethanol. *IV.* Modified the NDs on the tip surface. Before modification, The NDs were carboxylated using strong acid (mixture of H₂SO₄ and HNO₃ with 3:1 in volume) treatment, and the carboxylated NDs were dispersed in water with the aid of sonication treatment at least one hour. To activate the carboxyl groups on the NDs surface, the mixture of N-(dimethylaminopropyl)-N'-ethylcarbodiimide hydrochloride (EDC, 40 mg/mL) and N-hydroxysuccinimide (NHS, 10 mg/mL) with 1:1 volume ratio was added to the NDs dispersion. After 30 minutes, the aminated cone fiber tip was immersed in the carboxylated NDs dispersion to realize the modification of NDs on the tip surface via amidation reaction. Finally, the modified tip was rinsed using deionized water to remove the unbound NDs, and then dried at 100 °C, thus completing the fabrication of probe. In our experiments, different DCs and MDs were employed to explore the influence of these two parameters on the probe performance. In addition, in order to alleviate the impact of NDs aggregation, the NDs dispersion was sonicated for 10 minutes every 30 minutes during modification.

The employed fluorescence measurement setup for the probes was schematically-presented in Figure 1(j). The 532 nm pump light emitted from a laser (MGL-FN-532nm, CNI Optoelectronics Tech. Co.) was transmitted to the quantum probe through a fiber circulator (Thorlabs WMC3L1S) to excite the fluorescence of NDs. A part of the pump light and the emitted fluorescence from the NDs coupled back the fiber and went through the circulator. A 600 nm long-pass filter was used to isolate the excitation light, and finally, with the aid of an object lens, the remaining fluorescence signal was collected by a spectrometer (AvaSpec-ULS2048XL). For different probes, all test parameters were selected the same to ensure the comparability of test results.

To test the response of the probes to magnetic field via ODMR method, we improved the above setup to that shown in Figure 1(k). The MW, which was supplied from a MW source (Rohde & Schwarz SMB 100A) and amplified by an amplifier (Mini-Circuits ZHL-16W-43-S+), was applied on the probe through an antenna. The antenna was implemented by winding a copper wire (0.1 mm diameter) around the probe one cycle. Herein, we employed the lock-in amplifying technique to improve the test speed and signal to noise ratio²⁸. To implement this, the MW underwent a frequency modulation before emitted from the MW source, and a reference signal synchronized the modulation frequency was sent to the reference channel of a lock-in amplifier (LIA, Sine Scientific Instruments OE1022D), whose signal channel received the fluorescence signal

detected by the photodetector (Thorlabs APD410A/M). As a result, by sweeping the microwave frequency and recording the corresponding signal from LIA, we obtained a noise-reduced ODMR spectrum (we called it as LI-ODMR spectrum herein), which was the differential form of the normal spectrum shown in Figure 1(d).

RESULTS AND DISCUSSIONS

Magnetic field sensing

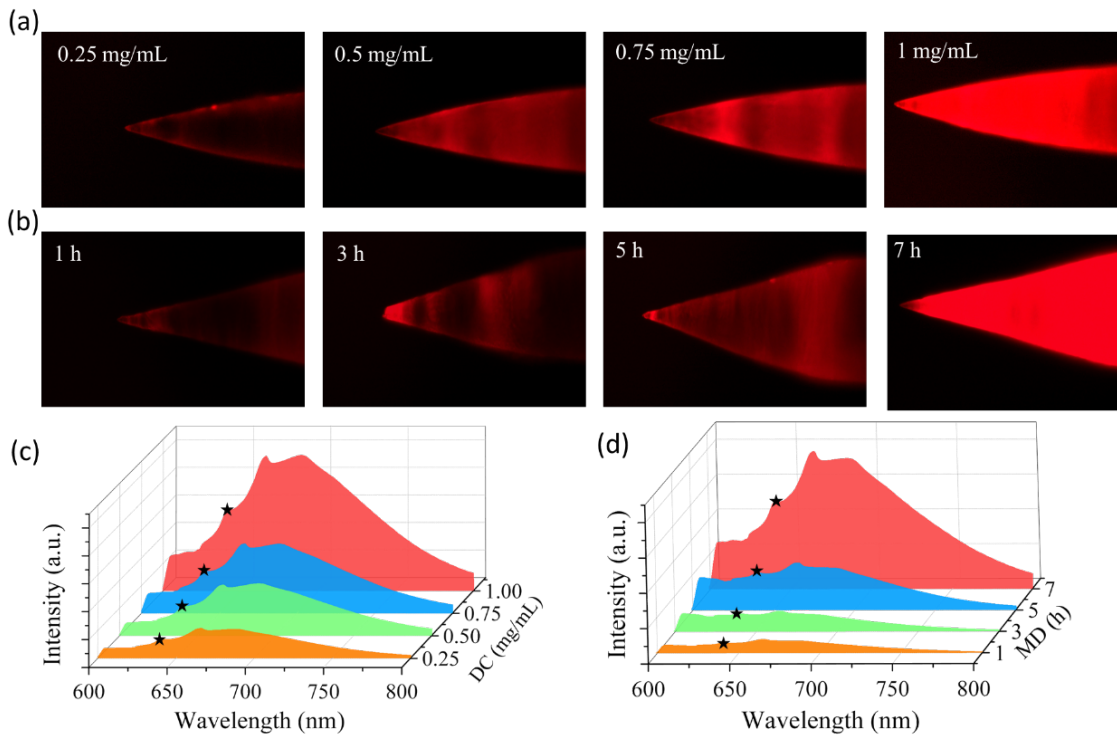


Figure 2. Fluorescence microscope images and corresponding fluorescence spectra of the probes. (a) and (c): the probes modified by different DCs and the same MD of 5 hours. (b) and (d): the probes modified by the same DC of 0.5 mg/mL and different MDs. In (c) and (d), the peaks at 637 nm indicated by the black stars correspond to the zero-phonon line of negatively-charged NV.

We first observed the probes, which were fabricated with different DCs and MDs, under a fluorescence microscope (MJ30 customized by adding a fluorescent module, Guangzhou Mshot Co.) using green light excitation and the same parameters. We can observe that the fluorescence emitted by the probe becomes stronger and stronger as the increase of DC and MD [as shown in Figures 2(a)-2(b)], though this part fluorescence fails to make contribution to the useful signal for sensing. To assess the fluorescence collected by the probe itself for sensing, the fluorescence spectra were measured by the setup shown in Figure 1(j). Likewise, the fluorescence that is coupled back fiber and collected by detector improves with the DC and MD, and all the spectra feature an obvious peak at 637 nm, corresponding to the zero-phonon line of negatively-charged NV [Figures 2(c)-2(d)]. All the above phenomena can be attributed to the increase of DC

or MD leading to more NDs modified on the conical fiber tip, thus generating a stronger fluorescence.

The LI-ODMR spectra of the probes and their responses to magnetic field variation were tested employing the experimental setup shown in Figure 1(k). Figure 3(a) indicates that as the increase of magnetic field variation, all the spectral lines are centered at 2.87 GHz while shifting to the both sides, which corresponds to the magnetic-field-induced split between $|+1\rangle$ and $|-1\rangle$ of NV ground stage. The center frequency ν_0 , corresponding to the zero-field split between $|0\rangle$ and $|\pm 1\rangle$, is temperature-dependent with a constant of about -74 kHz/K^{29} . During test, ν_0 almost remains unchanged for each probe with a maximal fluctuation of 0.16 MHz, suggesting a temperature variation of 2.2 K [Figure S1(a)]. The response of the resonance frequency ν_{\pm} to magnetic field variation, which is calculated by $R\nu_{\pm} = \text{abs}(\Delta\nu/\Delta B)$ for the probes with different DCs are presented in Figures S1(b)-S1(c), and it is indicated that the DC hardly affect the $R\nu_{\pm}$. This can be attributed to the following two facts: first, the NDs are randomly bond to the probe surface, making the NV axis distributed along every direction in equal probability; second, the split between $|+1\rangle$ and $|-1\rangle$ is essentially determined by the magnetic field projected along the NV axis rather than the number of NV centers.

However, the magnetic-electrical conversion coefficient, which is defined by the $R_s = \max|\Delta S(\nu) / \Delta B|$, i.e. the maximal change slope of the lock-in signal $S(\nu)$ within the whole magnetic field variation range ΔB is closely-related to the DC [Figure 2(b)]. The R_s had been enhanced from 2.83 to 15.36 V/T when the DC increased from 0.25 to 1 mg/mL. As shown by Figure 2(c), a higher DC corresponds to a stronger fluorescence, which results in a larger peak-valley contrast [Figure 3(a)], thus an improved R_s . To evaluate the magnetic field detection sensitivity of the probes, we first converted the electric noise $S_N(t)$ to magnetic noise $B_N(t)$ in time domain via $B_N(t) = S_N(t) / R_s$, where the $S_N(t)$ was acquired by consistently sampling the signal (at 1 kHz) from the lock-in amplifier for 60 s at an off-resonance MW frequency. Then, the magnetic noise amplitude spectral density (ASD) was calculated by the Welch's method². The results [Figure 3(c)] suggest that the detection sensitivity, defined as the magnetic noise spectral density at 1 Hz, improves with the DC, and it reaches $104.97 \text{ nT/Hz}^{1/2}$ when the DC increases to 1 mg/mL while MD is kept as 5 hours.

The influence of MD on the probe's magnetic field responses (including the resonance frequency shift, magnetic-electrical conversion coefficient, and detection sensitivity) shows the same laws as the DC (please see Figure S2 in supporting information for details). Using the 0.5 mg/mL DC, the magnetic-electrical coefficient is improved from 0.88 to 13.22 V/T when the MD rises from 1 to 7 hours [Figure 3(d)]. Correspondingly, the detection sensitivity is enhanced from 3121.79 to 191.22 $\text{nT/Hz}^{1/2}$ [Figure 3(e)].

To further enhance the magnetic detection sensitivity, a pair of magnetic flux concentrators (MFCs) were applied to the probes. The MFCs, which are usually made of high permeability materials and specially-designed in the shape, can collect the environmental magnetic flux and focus them to probes by an extremely-enhanced density³⁰, thus improving the sensibility to the environmental magnetic field. Herein, we employed two identical cone shape concentrators (base diameter 30 mm, tip diameter 0.8 mm, height 30 mm) made of permalloy (1J79, permeability 20000), and clamped the probe between the two concentrator tips with a distance 200 μm , as shown by Figure 3(f). For each probe modified by a given DC and MD, its magnetic field response is significantly-enhanced by the MFCs in all aspects, i.e. resonance frequency shift, magnetic-electrical coefficient, and detection sensitivity. Please see the Figures S4-S5 for details. We pick out and present the magnetic response of the probe that is modified by 1 mg/mL DC and 5 hours MD in Figures 3(g)-3(i). The magnetic-electrical coefficient and sensitivity have been improved to 1458.66 V/T and $0.57 \text{ nT/Hz}^{1/2}$, the highest ones obtained in our experiments. Figure 3(j) clearly presents the dependence of sensitivity on DC and MD, indicating about two orders of magnitude improvement in sensitivity induced by

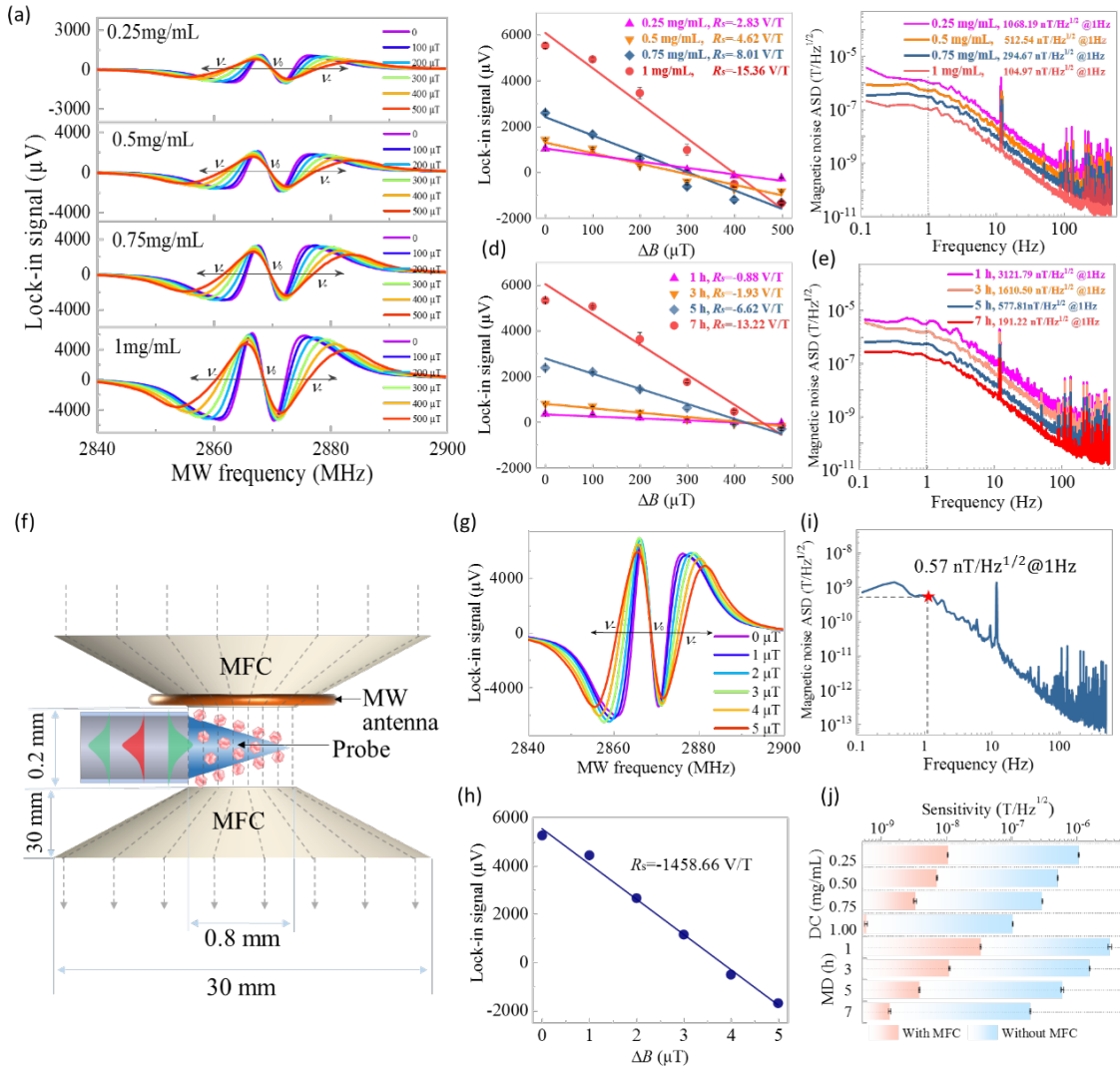


Figure 3. (a) Measured LI-ODMR spectral responses to the magnetic field variation, (b) magnetic-electrical conversion coefficients, and (c) magnetic noise ASD for the probes modified by different DCs and the same MD of 5 hours. (c) The magnetic-electrical conversion coefficients and (d) magnetic noise ASD for the probes modified by the same DC of 0.5 mg/mL and different MDs. (f) Schematic diagram for the application of a pair of MFCs to the probe and the arrangement form. The dash lines represent the magnetic induction lines. (g)-(i) Measured results of the magnetic field response after using MFCs for the 1 mg/mL DC and 7 hours MD probe. Note that the magnetic field variation range is 0-5 μT , scaled down by 100 times than the case without using MFCs. (j) Comparison in detection sensitivity with or without the use of MFCs for the various probes.

MFCs for each probe.

To prove the advantage of using a cone fiber tip, we prepared and measured the sensing performance of a probe with flat end face. At 1 mg/mL DC and 7 hours MD, magnetic-electrical coefficient and detection sensitivity for the flat-tip-based probe are 0.43 V/T and 8596 nT/Hz^{1/2} (Figure S5), which are much lower or poorer than those of the corresponding cone-tip-probe (1458.66 V/T and 0.57 nT/Hz^{1/2}) under the same conditions. This mainly arises from that the cone shape tip provides a larger surface to loading a larger amount of NDs, corresponding to a stronger fluorescence collected by fiber, when compared with the flat tip. Moreover, benefiting from the several measures taken in our work (including the special cone shape tip, the optimization on DC and MD, and the application of MFC), the sensitivity of 0.57 nT/Hz^{1/2} obtained herein shows a big improvement than those at $\mu\text{T}/\text{Hz}^{1/2}$ level obtained in other articles that also employ the fiber integrated with NDs scheme^{24,25,31,32}. At the same time, we can look forward to the further enhancement in sensitivity by optimizing the fiber cone parameters (such as the tip length and surface roughness) and the MFCs (in the aspects of materials, structure, size, etc.), which, however, are beyond the scope of this paper and will be presented in our other work.

Biosensing for paramagnetic species

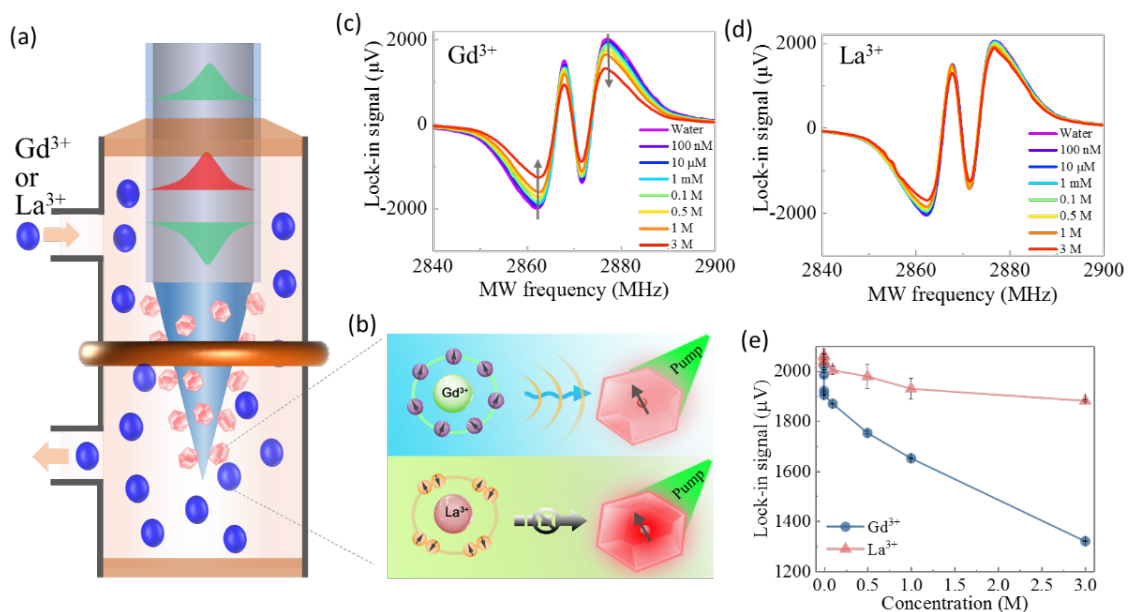


Figure 4. (a) Schematic depiction on the sensing to PS using a microfluidic tube. (b) Schematic illustration for the paramagnetic Gd³⁺ acting on the NV center via magnetic dipole while the non-paramagnetic La³⁺ showing no acting. (c)-(d) LI-ODMR spectrum depending on the concentration of Gd³⁺ and La³⁺, respectively. (e) The dependence of lock-in signal on the concentration at the fixed 2877 MHz MW frequency.

Paramagnetic species (PS) such as free radicals and paramagnetic metalloproteins, which contain one or more unpaired electrons in their valence shell, play crucial roles in various physiological processes including tumor growth³³, immune response³⁴, and metabolism³⁵, etc. Especially, increasing research suggests that endogenous PS have become the biomarkers for a variety of diseases^{36,37}. For example, the paramagnetic

metal accumulation in the deep gray matter nuclei was reported to be associated with the Wilson's disease recently³⁸. Reactive oxygen species free radicals have been implicated in an array of diseases including cancer, inflammation, and neurodegenerative diseases such as Parkinson's disease and Alzheimer's disease³⁹. Therefore, it is of great importance to sense the PS concentration via a suitable detection technology.

Herein, the following experiments were designed to demonstrate the potentials of our probes in detecting PS. As depicted in Figure 4(a), a probe was sealed in a microfluidic tube (with the inner/outer diameter of 2/3 mm) and the copper wire antenna was wound around the tube. Different concentrations of gadolinium nitrate [$\text{Gd}(\text{NO}_3)_3$] solutions were successively flowed through the tube, and the corresponding LI-ODMR spectra were recorded employing the same configuration shown in Figure 1(k). The Gd^{3+} , which was widely used as NMR contrast agent, possesses seven unpaired electron in the 4f subshell thus exhibiting strong paramagnetism. Considering that the magnetic spin noise generating from Gd^{3+} has a broadband spectral density extending to the GHz range, with frequency components corresponding to the NV Larmor precession, an affection from the surrounding Gd^{3+} will be exerted on the NV, which is consistently polarized to $|0\rangle$ by green laser pump, through the magnetic dipole coupling 10, as schematically-illustrated in Figure 4(b). This consequently reduces the $|0\rangle$ polarizability, manifesting as the decrease of the fluorescence emitted by NV under continue pump. As a control case, the same concentrations of lanthanum chloride (LaCl_3) solutions, where the La^{3+} is chemically similar to Gd^{3+} but it does not have any unpaired electrons (namely non-paramagnetic), were flowed through as well.

The measured results [Figures 4(c)-4(e)] well support the analysis as illustrated above. The contrast of the LI-ODMR spectrum, embodiment of the fluorescence intensity generated from NV under continue pump, exhibits significant dependence on the Gd^{3+} concentration while suffering little effect from La^{3+} . Specifically, as the increase of Gd^{3+} concentration, the contrast reduces obviously, but the resonant frequencies remain unchanged. The latter is attributed to the location of Gd^{3+} magnetic spin noise in the high frequency region (GHz), which affects the NV in a way of polarization reduction, rather than the detectable split of ground $|\pm 1\rangle$ induced by a static or slowly-varying magnetic field using the current continue-wave ODMR method. We also note a La^{3+} -related slight contrast variation, which is much smaller compared to the Gd^{3+} . This suggests that in our case of continue-wave ODMR, the magnetic spin noise (from the paramagnetic Gd^{3+}) plays a dominant role in the contrast reduction, whereas the another well-known process of charge state dynamic⁴⁰ that contributes to the La^{3+} -related slight contrast variation is suppressed. Based on the similar evaluation method for sensitivity as the magnetic field, the detection sensitivity for Gd^{3+} is evaluated as $26.8 \text{ nM/Hz}^{1/2}$ (Figure S6).

In a word, we demonstrated a novel scheme for PS detection using an optical-fiber quantum probe featuring high integration, small size, and high sensitivity. Moreover, the employed lock-in technique and ODMR method enable us to acquire the results with high signal-to-noise ratio in a short time (hundreds of milliseconds), which shows a big advantage when compared with the longitudinal relaxation (T_1) measurement method (generally needs a few minutes even more)^{9,35}. Therefore, the method presented here holds great potentials in studying the PS-related physiological or chemical dynamic processes within a local region. It should be pointed out that the current work focuses to demonstrate the capability of the proposed probe in PS sensing, the further work aimed at specificity and mechanism clarity is necessary before practical application.

CONCLUSIONS

In summary, a novel configuration to exploiting NV centers in diamond as a quantum probe is proposed and demonstrated. The probe is implemented by anchoring the nanodiamonds containing NV centers onto a cone fiber tip via chemical covalent bonding, and it is applied to the sensing to magnetic field and PS based on the continue-wave ODMR method and lock-in amplifying technique. Through experimental measurements, it is found that both of the DC and MD have little influence on the responses of center and resonant frequencies to the magnetic field variation. Whereas, the magnetic-electrical conversion coefficient and detection sensitivity are closely-related to the DC and MD. Increasing DC and MD is beneficial to the improvement of magnetic detection sensitivity, because more NDs can be modified on the fiber tip thus enhancing the fluorescence signal. Additionally, after applying a pair of MFCs to the probe, the sensitivity succeeds to be further enhanced with two orders of magnitude. The highest sensitivity of $0.57 \text{ nT/Hz}^{1/2}$ @ 1Hz had been achieved in our experiments, and we can look forward to a further enhancement by optimizing the fiber cone parameters (tip length, surface roughness, etc.) and the MFCs (in the aspects of materials, structure, size, etc.). The probe also exhibits great potentials in biosensing to PS, which was demonstrated by a well-designed experiment where the probe was much sensitive to the paramagnetic Gd^{3+} but little affected by the non-paramagnetic La^{3+} . The detection sensitivity for Gd^{3+} was achieved as $26.8 \text{ nM/Hz}^{1/2}$ in experiments. Our work paves the way to the development of optical-fiber based quantum probe featuring high integration, miniature size, multifunction, and high sensitivity.

Supporting Information

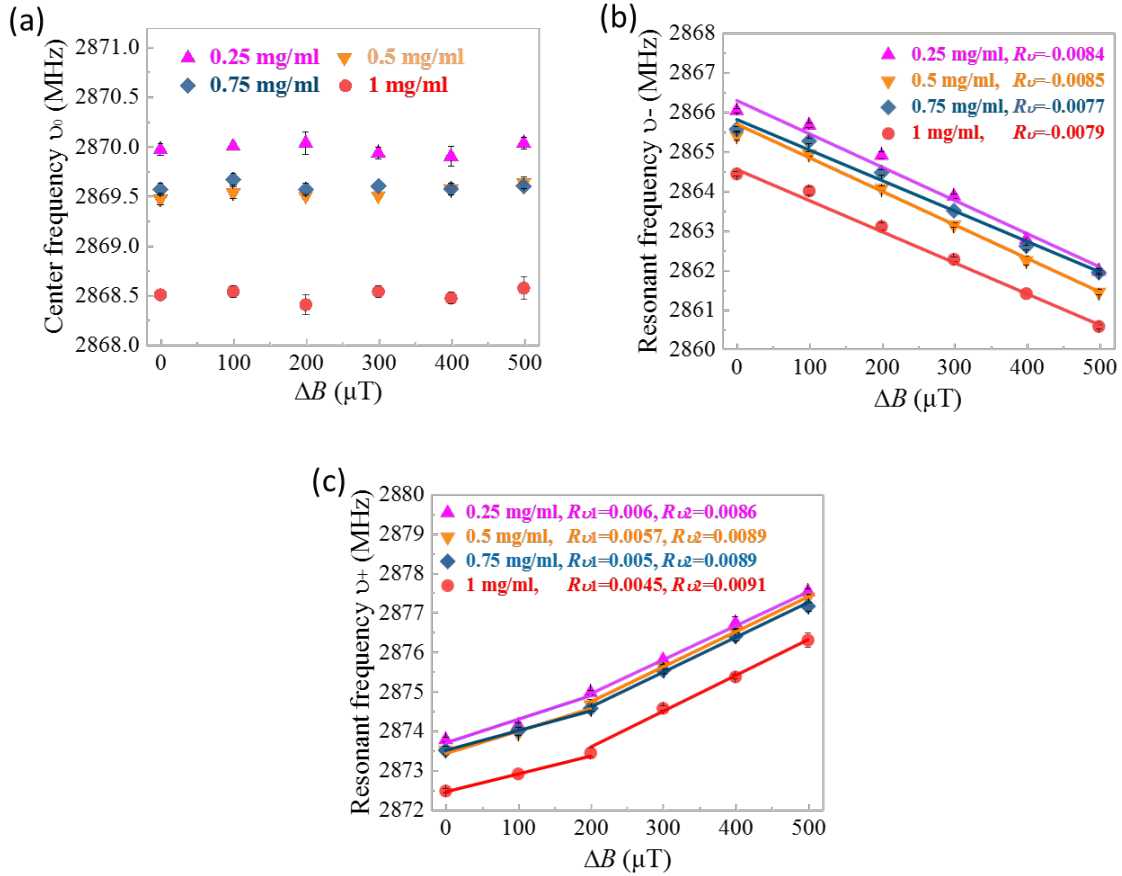


Figure S1. Center and resonant frequencies dependence on the magnetic field variation for the probes with different DCs and the same MD of 5 hours. (a) Center frequency ν_0 . The maximal deviation of 0.16 MHz occurs between the ΔB at 200 and 500 μT for the probe with DC 1 mg/mL, corresponding to a temperature variation of 2.2 K according the temperature-dependent constant of about -74 kHz/K^{29} . The ν_0 deviation among the probes, the maximum of 1.5 MHz occurring between the probes with DC 0.25 and 1 mg/mL, is mainly due to the temperature variation and measurement error during experiments, and the variations in static local strain and transverse magnetic field in NDs for the different probes⁴¹. (b) Resonant frequency R_{ν_-} . The linear fitting results show that the $R_{\nu_-} = \text{abs}(\Delta \nu_- / \Delta B)$ are 0.0084, 0.0085, 0.0077, and 0.0079 MHz/ μT , with a maximal deviation of 8.3%, for the probes with different DCs. This suggests that the DC has little influence on the response of ν_- to magnetic field, namely R_{ν_-} . (c) Resonant frequency ν_+ . The linear fitting results show that the $R_{\nu_+} = \text{abs}(\Delta \nu_+ / \Delta B)$ are almost equal for the probes with different DCs. This suggests that the DC also has little influence on the response of ν_+ to magnetic field, namely R_{ν_+} .

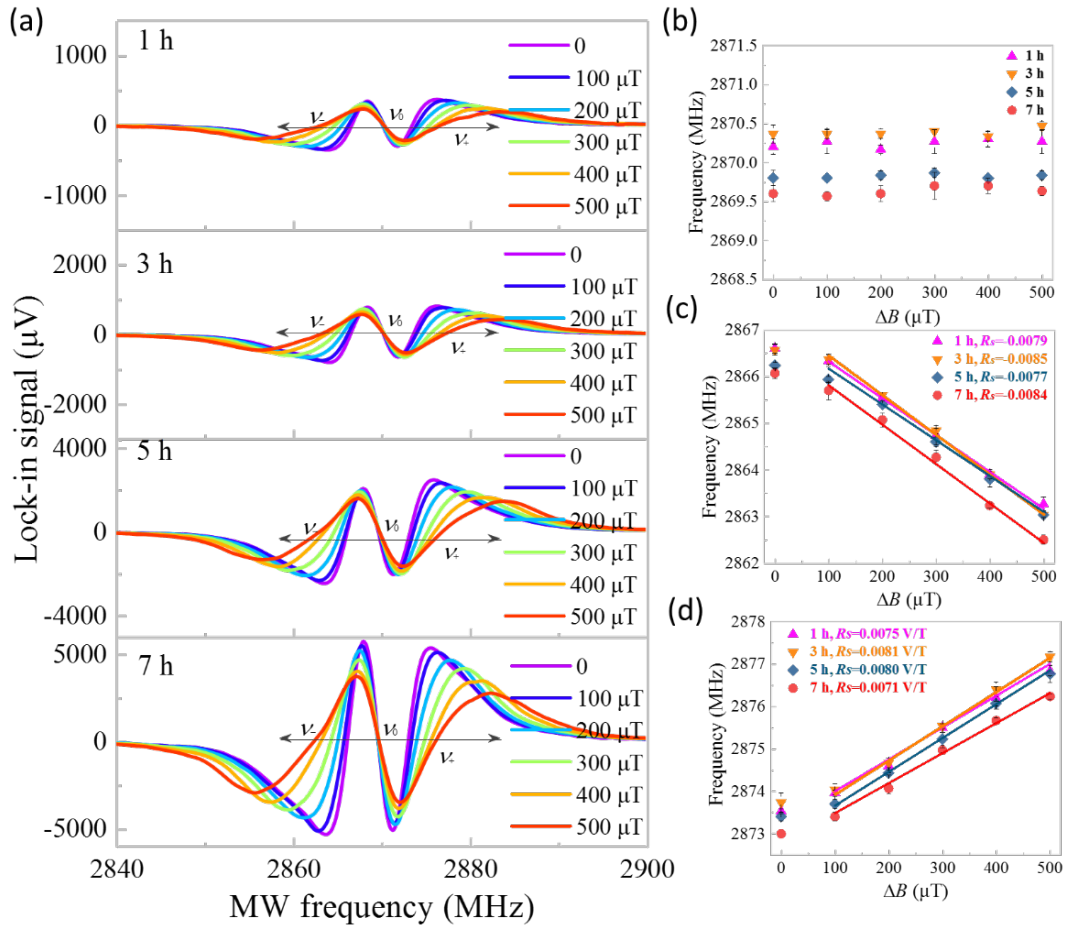


Figure S2. (a) Measured LI-ODMR spectral responses to the magnetic field variation for the probes modified by the same DC of 0.5 mg/mL and different MDs. Similarly, as the increase of magnetic field, all the spectral lines are centered at 2.87GHz while shifting to the opposite sides. Meanwhile, the peak-valley contrast increases as well, which corresponds to a stronger fluorescence at a larger MD as shown by Figure 2(c). Therefore, both the magnetic-electrical conversion coefficient and detection sensitivity improve with the MD, as shown in Figure 3(d)-3(e). (b) Center frequency ν_0 , (c) resonant frequency R_{ν_-} , and (d) resonant frequency ν_+ dependence on the magnetic field variation for the different probes. The similar conclusions as illustrated by the above Figure S1 can be obtained: the temperature-dependent center frequency ν_0 remains almost unchanged during the test for each probe; the MD has little influence on the response of the resonant frequencies ν_+ and R_{ν_-} to magnetic field variation.

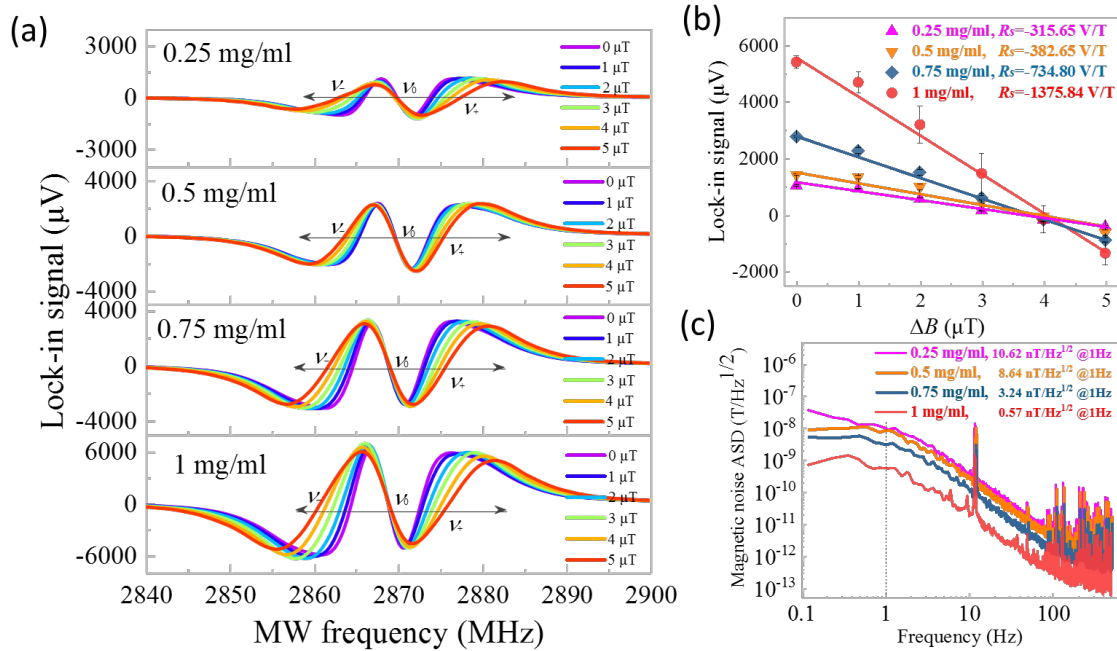


Figure S3. After using MFCs, the measured responses to magnetic field variation for the probes with the different DCs and the same MD of 5 hours. (a) LI-ODMR spectral responses to the magnetic field variation. Note that though the magnetic field variation range is scaled down 100 times (i.e. 0-5 μT) when compared to case without using MFCs (i.e. 0-500 μT), the significant spectral response can be observed. (b)-(c) Magnetic-electrical conversion coefficients and magnetic noise ASD for each probe. These two performance indicators both have improvement by two orders of magnitude after using MFCs, compared with the results in Figures 3(b)-3(c).

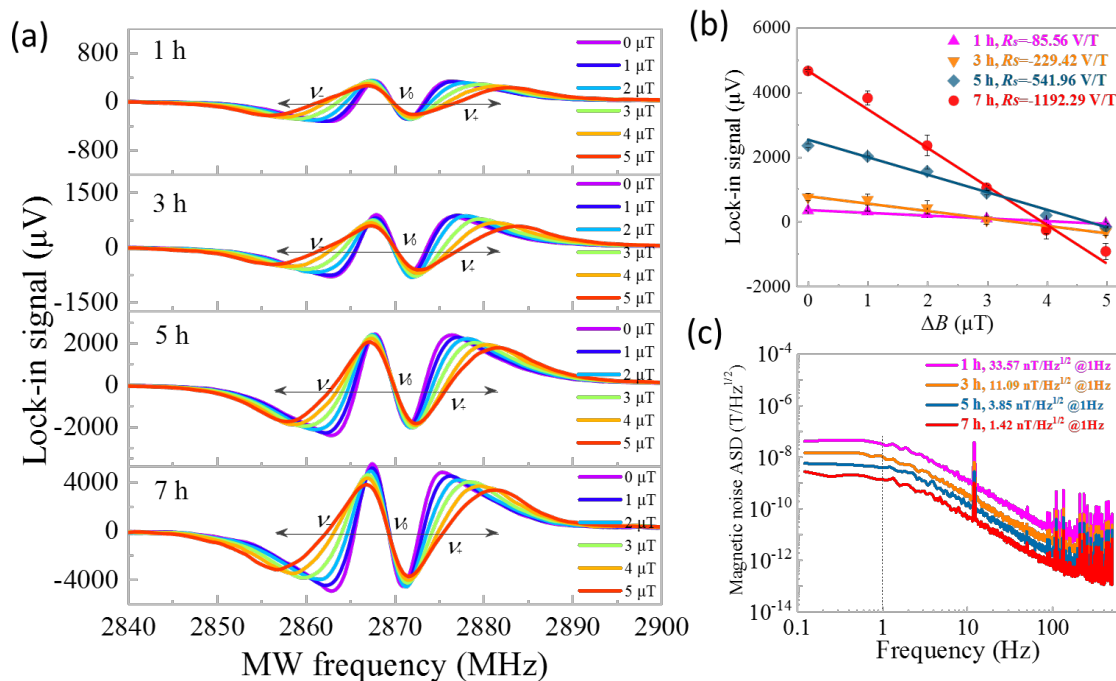


Figure S4. After using MFCs, the measured responses to magnetic field variation for the probes with the same DC of 0.5 mg/mL and the different MDs. (a) LI-ODMR spectral responses to the magnetic field variation. Note that though the magnetic field variation range is scaled down 100 times (i.e. 0-5 μT) when compared to case without using MFCs (i.e. 0-500 μT), the significant spectral response can be observed. (b)-(c) Magnetic-electrical conversion coefficients and magnetic noise ASD for each probe. These two performance indicators both have improvement by two orders of magnitude after using MFCs, compared with the results in Figures 3(d)-3(e).

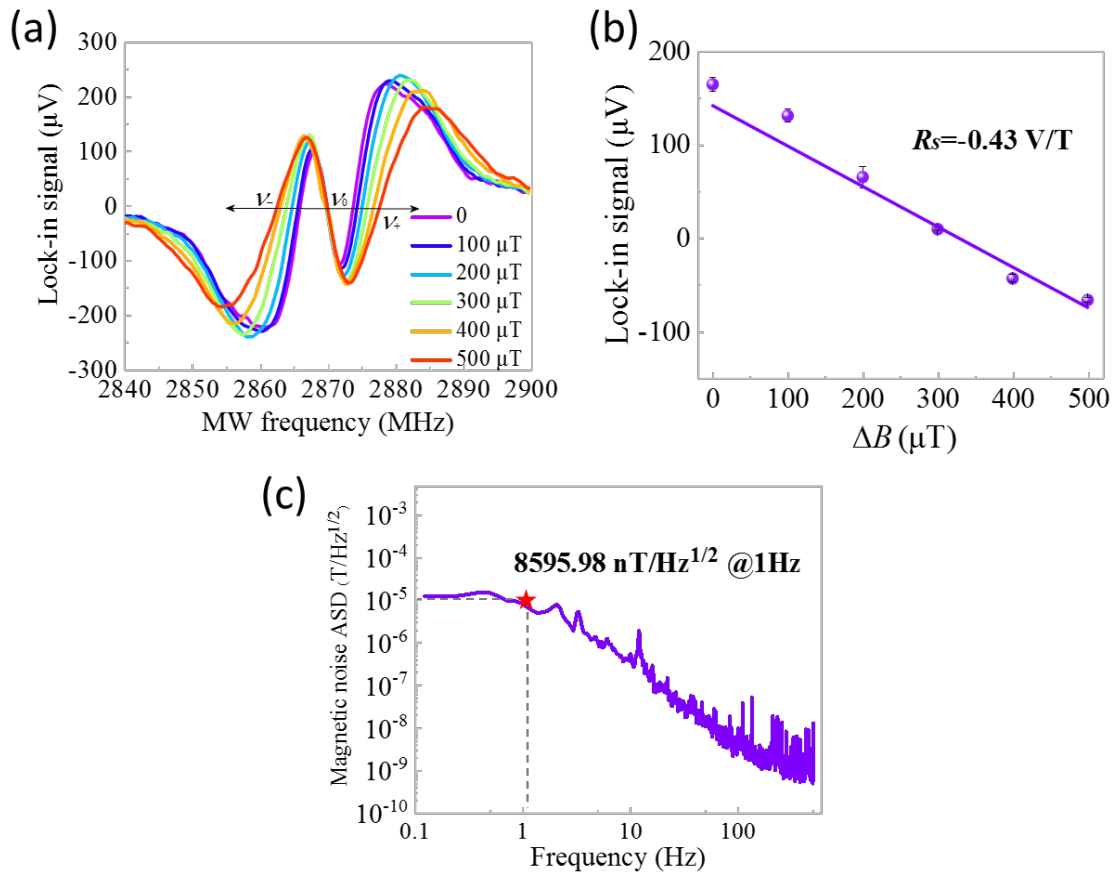


Figure S5. Measured magnetic field sensing results for the fiber probe with a flat end face modified by 1 mg/mL DC and 7 hours MD. (a) LI-ODMR spectral responses to the magnetic field variation. (b) Measured magnetic-electrical conversion coefficient and (c) magnetic noise ASD for the probe. Note that though the LI-ODMR spectrum exhibits the same magnetic-response behaviors, i.e. centered at 2.87GHz while shifting to the opposite sides as the increase of magnetic field variation, the peak-valley contrast is significantly-reduced when compared with the cone-tip probe fabricated at the same conditions. Correspondingly, both the magnetic-electrical conversion coefficient and the detection sensitivity have deteriorated.

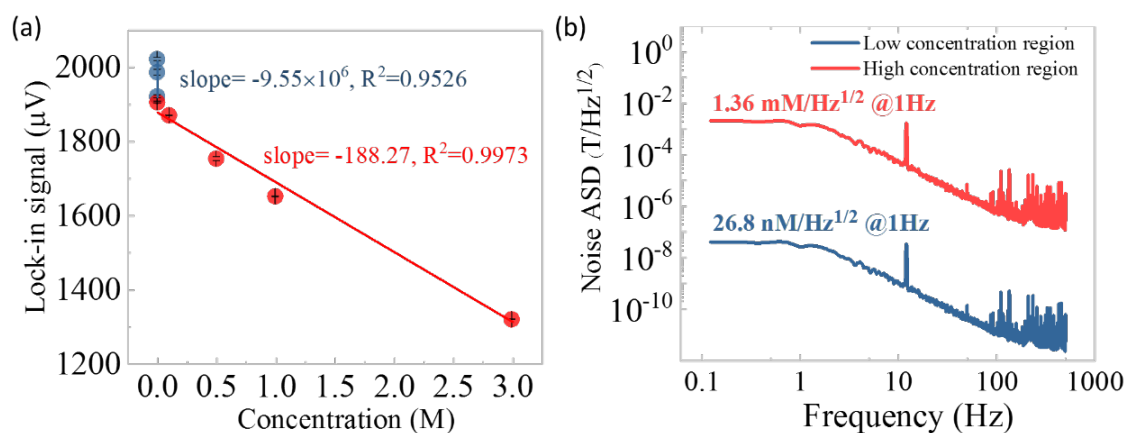


Figure S6. (a) Linear fittings of the measured data for Gd^{3+} at the linear regions. The obtained responsivity are $-9.55 \times 10^6 \mu\text{V}/\text{M}$ and $-188.27 \mu\text{V}/\text{M}$ at the low and high concentration regions. (b) Noise ASD for the Gd^{3+} detection. The noise ASD herein is obtained through Welch's method same as the evaluation for magnetic noise ASD presented in text. Results indicate that the probe has the detection sensitivities of $26.8 \text{ nM}/\text{Hz}^{1/2}$ and $1.36 \text{ mM}/\text{Hz}^{1/2}$ at the low ($0\text{-}10 \mu\text{M}$) and high ($1\text{mM}\text{-}3\text{M}$) concentration regions, respectively.

ASSOCIATED CONTENT

ORCID

Yaofei Chen: 0000-0002-7067-6562
Yunhan Luo: 0000-0002-6587-832X

Notes

The author declare no competing financial interest.

Acknowledgments

This work is supported by the National Natural Science Foundation of China (NSFC) (61805108, 62175094, 61904067, 62075088); Guangdong Basic and Applied Basic Research Foundation (2020A1515011498, 2017A010101013); Science & Technology Project of Guangzhou (201707010500, 201807010077, 201704030105, 201605030002); Science and Technology R&D Project of Shenzhen (JSGG20201102163800003, JSGG20210713091806021); Fundamental Research Funds for the Central Universities (21620328).

References

1. H. C. Chang, W. W. Hsiao, and M. C. Su. Fluorescent nanodiamonds || producing fluorescent nanodiamonds. *Fluorescent Nanodiamonds*, 10.1002/9781119477099:91–112, 2018.
2. Yijin Xie, Huiyao Yu, Yunbin Zhu, Xi Qin, Xing Rong, Chang-Kui Duan, and Jiangfeng Du. A hybrid magnetometer towards femtotesla sensitivity under ambient conditions. *Science Bulletin*, 66(2):127–132, 2021.
3. Hannah Clevenson, Linh M Pham, Carson Teale, Kerry Johnson, Dirk Englund, and Danielle Braje. Robust high-dynamic-range vector magnetometry with nitrogen-vacancy centers in diamond. *Applied Physics Letters*, 112(25):252406, 2018.
4. Shingo Sotoma, Chongxia Zhong, James Chen Yong Kah, Hayato Yamashita, Taras Plakhotnik, Yoshie Harada, and Madoka Suzuki. In situ measurements of intracellular thermal conductivity using heater-thermometer hybrid diamond nanosensors. *Science advances*, 7(3):eabd7888, 2021.
5. Tongtong Zhang, Goutam Pramanik, Kai Zhang, Michal Gulka, Lingzhi Wang, Jixiang Jing, Feng Xu, Zifu Li, Qiang Wei, Petr Cigler, et al. Toward quantitative bio-sensing with nitrogen–vacancy center in diamond. *ACS sensors*, 6(6):2077–2107, 2021.
6. Yuen Yung Hui, Oliver J Chen, Hsin-Hung Lin, Yu-Kai Su, Katherine Y Chen, Chih-Yen Wang, Wesley W-W Hsiao, and Huan-Cheng Chang. Magnetically modulated fluorescence of nitrogen-vacancy centers in nanodiamonds for ultrasensitive biomedical analysis. *Analytical Chemistry*, 93(18):7140–7147, 2021.
7. Benjamin S Miller, Leonard Bezing, Harriet D Gliddon, Da Huang, Gavin Dold, Eleanor R Gray, Judith Heaney, Peter J Dobson, Eleni Nastouli, John JL Morton, et al. Spin-enhanced nanodiamond biosensing for ultrasensitive diagnostics. *Nature*, 587(7835):588–593, 2020.
8. Yoav Ninio, Nir Waiskopf, Idan Meirzada, Yoav Romach, Galya Haim, Shira Yochelis, Uri Banin, and Nir Bar-Gill. High-sensitivity, high-resolution detection of reactive oxygen species concentration using nv centers. *ACS Photonics*, 8(7):1917–1921, 2021.
9. Felipe Perona Martinez, Anggrek Citra Nusantara, Mayeul Chipaux, Sandeep Kumar Padamati, and Romana Schirhagl. Nanodiamond relaxometry-based detection of free-radical species when produced in chemical reactions in biologically relevant conditions. *ACS sensors*, 5(12):3862–3869, 2020.
10. Valentin Radu, Joshua Colm Price, Simon James Levett, Kaarjel Kauslya Narayanasamy, Thomas David Bateman-Price, Philippe Barrie Wilson, and Melissa Louise Mather. Dynamic quantum sensing of paramagnetic species using nitrogen-vacancy centers in diamond. *ACS sensors*, 5(3):703–710, 2019.
11. Takahiro Fujisaku, Ryotaro Tanabe, Shinobu Onoda, Ryou Kubota, Takuya F Segawa, Frederick T-K So, Takeshi Ohshima, Itaru Hamachi, Masahiro Shirakawa, and Ryuji Igarashi. ph nanosensor using electronic spins in diamond. *ACS nano*, 13(10):11726–11732, 2019.
12. Helena Raabova, David Chvatil, and Petr Cigler. Diamond nano-optode for fluorescent measurements of ph and temperature. *Nanoscale*, 11(40):18537–18542, 2019.

13. Torsten Rendler, Jitka Neburkova, Ondrej Zemek, Jan Kotek, Andrea Zappe, Zhiqin Chu, Petr Cigler, and Jörg Wrachtrup. Optical imaging of localized chemical events using programmable diamond quantum nanosensors. *Nature communications*, 8(1):1–9, 2017.
14. Jan Barton, Michal Gulka, Jan Tarabek, Yuliya Mindarava, Zhenyu Wang, Jiri Schimer, Helena Raabova, Jan Bednar, Martin B Plenio, Fedor Jelezko, et al. Nanoscale dynamic readout of a chemical redox process using radicals coupled with nitrogen-vacancy centers in nanodiamonds. *ACS nano*, 14(10):12938–12950, 2020.
15. Dominik B Bucher, Diana PL Aude Craik, Mikael P Backlund, Matthew J Turner, Oren Ben Dor, David R Glenn, and Ronald L Walsworth. Quantum diamond spectrometer for nanoscale nmr and esr spectroscopy. *Nature Protocols*, 14(9):2707–2747, 2019.
16. Donggyu Kim, Mohamed I Ibrahim, Christopher Foy, Matthew E Trusheim, Ruonan Han, and Dirk R Englund. A cmos-integrated quantum sensor based on nitrogen–vacancy centres. *Nature Electronics*, 2(7):284–289, 2019.
17. James L Webb, Joshua D Clement, Luca Troise, Sepehr Ahmadi, Gustav Juhl Johansen, Alexander Huck, and Ulrik L Andersen. Nanotesla sensitivity magnetic field sensing using a compact diamond nitrogen-vacancy magnetometer. *Applied Physics Letters*, 114(23):231103, 2019.
18. IV Fedotov, SM Blakley, EE Serebryannikov, P Hemmer, MO Scully, and AM Zheltikov. High-resolution magnetic field imaging with a nitrogen-vacancy diamond sensor integrated with a photonic-crystal fiber. *Optics Letters*, 41(3):472–475, 2016.
19. SM Blakley, IV Fedotov, J Becker, and AM Zheltikov. Quantum stereomagnetometry with a dual-core photonic-crystal fiber. *Applied Physics Letters*, 113(1):011112, 2018.
20. Dewen Duan, Vinaya Kumar Kavatamane, Sri Ranjini Arumugam, Yan-Kai Tzeng, Huan-Cheng Chang, and Gopalakrishnan Balasubramanian. Tapered ultra-high numerical aperture optical fiber tip for nitrogen vacancy ensembles based endoscope in a fluidic environment. *Applied Physics Letters*, 116(11):113701, 2020.
21. Felix M Stürner, Andreas Brenneis, Thomas Buck, Julian Kassel, Robert Rölver, Tino Fuchs, Anton Savitsky, Dieter Suter, Jens Grimmel, Stefan Hengeshbach, et al. Integrated and portable magnetometer based on nitrogen-vacancy ensembles in diamond. *Advanced Quantum Technologies*, 4(4):2000111, 2021.
22. Shao-Chun Zhang, Yang Dong, Bo Du, Hao-Bin Lin, Shen Li, Wei Zhu, Guan-Zhong Wang, Xiang-Dong Chen, Guang-Can Guo, and Fang-Wen Sun. A robust fiber-based quantum thermometer coupled with nitrogen-vacancy centers. *Review of Scientific Instruments*, 92(4):044904, 2021.
23. Shai Maayani, Christopher Foy, Dirk Englund, and Yoel Fink. Distributed quantum fiber magnetometry. *Laser & Photonics Reviews*, 13(7):1900075, 2019.
24. Xiaodi Liu, Jinming Cui, Fangwen Sun, Xuerui Song, Fupan Feng, Junfeng Wang, Wei Zhu, Liren Lou, and Guanzhong Wang. Fiber-integrated diamond-based magnetometer. *Applied Physics Letters*, 103(14):143105, 2013.

-
25. IV Fedotov, LV Doronina-Amitonova, DA Sidorov-Biryukov, NA Safronov, AO Levchenko, SA Zibrov, S Blakley, H Perez, AV Akimov, AB Fedotov, et al. Fiber-optic magnetometry with randomly oriented spins. *Optics Letters*, 39(23):6755–6758, 2014.
 26. Tristan Petit and Ljiljana Puskar. Ftir spectroscopy of nanodiamonds: Methods and interpretation. *Diamond and Related Materials*, 89:52–66, 2018.
 27. L Rondin, G Dantelle, A Slablab, F Grosshans, F Treussart, P Bergonzo, S Perruchas, T Gacoin, M Chaigneau, H-C Chang, et al. Surface-induced charge state conversion of nitrogen-vacancy defects in nanodiamonds. *Physical Review B*, 82(11):115449, 2010.
 28. Rolf Simon Schoenfeld and Wolfgang Harneit. Real time magnetic field sensing and imaging using a single spin in diamond. *Physical review letters*, 106(3):030802, 2011.
 29. Yingke Wu, Md Noor A Alam, Priyadharshini Balasubramanian, Anna Ermakova, Stephan Fischer, Holger Barth, Manfred Wagner, Marco Raabe, Fedor Jelezko, and Tanja Weil. Nanodiamond theranostic for light-controlled intracellular heating and nanoscale temperature sensing. *Nano Letters*, 21(9):3780–3788, 2021.
 30. Ilja Fescenko, Andrey Jarmola, Igor Savukov, Pauli Kehayias, Janis Smits, Joshua Damron, Nathaniel Ristoff, Nazanin Mosavian, and Victor M Acosta. Diamond magnetometer enhanced by ferrite flux concentrators. *Physical review research*, 2(2):023394, 2020.
 31. Yinlan Ruan, David A Simpson, Jan Jeske, Heike Ebendorff-Heidepriem, Desmond WM Lau, Hong Ji, Brett C Johnson, Takeshi Ohshima, Shahraam Afshar V, Lloyd Hollenberg, et al. Magnetically sensitive nanodiamond-doped tellurite glass fibers. *Scientific reports*, 8(1):1–6, 2018.
 32. Dongbi Bai, Minh Hoa Huynh, David A Simpson, Philipp Reineck, S Afshar Vahid, Andrew D Greentree, Scott Foster, H Ebendorff-Heidepriem, and BC Gibson. Fluorescent diamond microparticle doped glass fiber for magnetic field sensing. *APL Materials*, 8(8):081102, 2020.
 33. Gang Cheng, Jing Pan, Radoslaw Podsiadly, Jacek Zielonka, Alexander M Garces, Luiz Gabriel Dias Duarte Machado, Brian Bennett, Donna McAllister, Michael B Dwinell, Ming You, et al. Increased formation of reactive oxygen species during tumor growth: Ex vivo low-temperature epr and in vivo bioluminescence analyses. *Free radical biology and medicine*, 147:167–174, 2020.
 34. Bruna RB Gomes, Marina Firmino, Jardeson S Jorge, Maria LO Ferreira, Thays M Rodovalho, Simone N Weis, Gloria EP Souza, Paulo C Morais, Marcelo V Sousa, Paulo EN Souza, et al. Increase of reactive oxygen species in different tissues during lipopolysaccharide-induced fever and antipyresis: an electron paramagnetic resonance study. *Free radical research*, 52(3):351–361, 2018.
 35. L Nie, AC Nusantara, VG Damle, R Sharmin, EPP Evans, SR Hemelaar, KJ Van der Laan, R Li, FP Perona Martinez, T Vedelaar, et al. Quantum monitoring of cellular metabolic activities in single mitochondria. *Science advances*, 7(21):eabf0573, 2021.
 36. Aya Umeno, Vasudevanpillai Biju, and Yasukazu Yoshida. In vivo ros production and use of oxidative stress-derived biomarkers to detect the onset of diseases such as alzheimer’s disease, parkinson’s disease, and diabetes. *Free Radical Research*, 51(4):413–427, 2017.

-
37. Xiao-Qiang Wang, Wenjing Wang, Mengyun Peng, and Xian-Zheng Zhang. Free radicals for cancer theranostics. *Biomaterials*, 266:120474, 2021.
 38. Xiang-Zhen Yuan, Gai-Ying Li, Jia-Lin Chen, Jian-Qi Li, and Xiao-Ping Wang. Paramagnetic metal accumulation in the deep gray matter nuclei is associated with neurodegeneration in wilson's disease. *Frontiers in neuroscience*, page 993, 2020.
 39. Kai-Cheng Yan, Adam C Sedgwick, Yi Zang, Guo-Rong Chen, Xiao-Peng He, Jia Li, Juyoung Yoon, and Tony D James. Sensors, imaging agents, and theranostics to help understand and treat reactive oxygen species related diseases. *Small Methods*, 3(7):1900013, 2019.
 40. F Gorrini, R Giri, CE Avalos, S Tambalo, S Mannucci, L Basso, N Bazzanella, C Dorigoni, M Cazzanelli, P Marzola, et al. Fast and sensitive detection of paramagnetic species using coupled charge and spin dynamics in strongly fluorescent nanodiamonds. *ACS applied materials & interfaces*, 11(27):24412–24422, 2019.
 41. Arne Barfuss, Jean Teissier, Elke Neu, Andreas Nunnenkamp, and Patrick Maletinsky. Strong mechanical driving of a single electron spin. *Nature Physics*, 11(10):820–824, 2015.